In vivo studies of transdermal nanoparticle delivery with microneedle using photoacoustic microscopy

Moothanchery, Mohesh; Seeni, Razina Z.; Xu, Chenjie; Pramanik, Manojit

2017

Moothanchery, M., Seeni, R. Z., Xu, C., & Pramanik, M. (2017). In vivo studies of transdermal nanoparticle delivery with microneedles using photoacoustic microscopy. Biomedical Optics Express, 8(12), 5483-5492.

https://hdl.handle.net/10356/86332

https://doi.org/10.1364/BOE.8.005483

In vivo studies of transdermal nanoparticle delivery with microneedles using photoacoustic microscopy

MOHESH MOOTHANCHERY,[†1] RAZINA Z. SEENI,[†1] CHENJIE XU,[1,2,3*] MANOJIT PRAMANIK[1*]

[1]*School of Chemical and Biomedical Engineering, Nanyang Technological University, 62 Nanyang Drive, Singapore 637459*
[2]*NTU-Northwestern Institute for Nanomedicine, Nanyang Technological University, 50 Nanyang Avenue, 639798, Singapore.*
[3]*cjxu@ntu.edu.sg*
[†]*Both authors contributed equally*

**manojit@ntu.edu.sg*

Abstract: Microneedle technology allows micron-sized conduits to be formed within the outermost skin layers for both localized and systemic delivery of therapeutics including nanoparticles. Histological methods are often employed for characterization, and unfortunately do not allow for the *in vivo* visualization of the delivery process. This study presents the utilization of optical resolution-photoacoustic microscopy to characterize the transdermal delivery of nanoparticles using microneedles. Specifically, we observe the *in vivo* transdermal delivery of gold nanoparticles using microneedles in mice ear and study the penetration, diffusion, and spatial distribution of the nanoparticles in the tissue. The promising results reveal that photoacoustic microscopy can be used as a potential imaging modality for the *in vivo* characterization of microneedles based drug delivery.

OCIS codes: (110.5120) Photoacoustic Imaging; (110.5125) Photoacoustics; (170.0180) Microscopy; (170.5180) Photodynamic therapy; (160.4236) Nanomaterials;

References and links

1. Y. Lu, A. A. Aimetti, R. Langer, and Z. Gu, "Bioresponsive materials," Nature Reviews Materials **2**, 16075 (2016).
2. M. R. Prausnitz, "Microneedles for transdermal drug delivery," Advanced Drug Delivery Reviews **56**, 581-587 (2004).
3. K. van der Maaden, W. Jiskoot, and J. Bouwstra, "Microneedle technologies for (trans)dermal drug and vaccine delivery," J. Control. Release **161**, 645-655 (2012).
4. M. Wang, L. Hu, and C. Xu, "Recent advances in the design of polymeric microneedles for transdermal drug delivery and biosensing," Lab on a Chip **17**, 1373-1387 (2017).
5. R. Liu, M. Zhang, and C. Jin, "In vivo and in situ imaging of controlled-release dissolving silk microneedles into the skin by optical coherence tomography," Journal of biophotonics **10**, 870-877 (2016).
6. R. F. Donnelly, M. J. Garland, D. I. Morrow, K. Migalska, T. R. Singh, R. Majithiya, and A. D. Woolfson, "Optical coherence tomography is a valuable tool in the study of the effects of microneedle geometry on skin penetration characteristics and in-skin dissolution," J. Control. Release **147**, 333-341 (2010).
7. J. Enfield, M. L. O'Connell, K. Lawlor, E. Jonathan, C. O'Mahony, and M. Leahy, "In-vivo dynamic characterization of microneedle skin penetration using optical coherence tomography," J. Biomed. Opt. **15**, 046001 (2010).
8. R. Z. Seeni, X. Yu, H. Chang, P. Chen, L. Liu, and C. Xu, "Iron Oxide Nanoparticle-Powered Micro-Optical Coherence Tomography for in Situ Imaging the Penetration and Swelling of Polymeric Microneedles in the Skin," ACS Applied Materials & Interfaces **9**, 20340-20347 (2017).

9. M.-T. Tsai, I. C. Lee, Z.-F. Lee, H.-L. Liu, C.-C. Wang, Y.-C. Choia, H.-Y. Chou, and J.-D. Lee, "In vivo investigation of temporal effects and drug delivery induced by transdermal microneedles with optical coherence tomography," Biomedical Optics Express **7**, 1865-1876 (2016).
10. R. F. Donnelly, M. J. Garland, D. I. J. Morrow, K. Migalska, T. R. R. Singh, R. Majithiya, and A. D. Woolfson, "Optical coherence tomography is a valuable tool in the study of the effects of microneedle geometry on skin penetration characteristics and in-skin dissolution," Journal of Controlled Release **147**, 333-341 (2010).
11. M. Moothanchery and M. Pramanik, "Performance Characterization of a Switchable Acoustic Resolution and Optical Resolution Photoacoustic Microscopy System," Sensors **17**, 357 (2017).
12. Y. Zhou, J. Yao, and L. V. Wang, "Tutorial on photoacoustic tomography," J. Biomed. Opt. **21**, 061007 (2016).
13. L. V. Wang and J. Yao, "A practical guide to photoacoustic tomography in the life sciences," Nat Methods **13**, 627-638 (2016).
14. S. Manohar and D. Razansky, "Photoacoustics: a historical review," Advances in Optics and Photonics **8**, 586-617 (2016).
15. J. Yao and L. V. Wang, "Photoacoustic Brain Imaging: from Microscopic to Macroscopic Scales," Neurophotonics **1**, 011003 (2014).
16. L. V. Wang and S. Hu, "Photoacoustic Tomography: In Vivo Imaging from Organelles to Organs," Science **335**, 1458-1462 (2012).
17. S. Hu, K. Maslov, and L. V. Wang, "Second-generation optical-resolution photoacoustic microscopy with improved sensitivity and speed," Opt. Lett. **36**, 1134-1136 (2011).
18. J. Yao, A. A. Kaberniuk, L. Li, D. M. Shcherbakova, R. Zhang, L. Wang, G. Li, V. V. Verkhusha, and L. V. Wang, "Multiscale photoacoustic tomography using reversibly switchable bacterial phytochrome as a near-infrared photochromic probe," Nat Methods **13**, 67-73 (2016).
19. P. Beard, "Biomedical photoacoustic imaging," Interface Focus **1**, 602-631 (2011).
20. D. Pan, M. Pramanik, A. Senpan, S. Ghosh, S. A. Wickline, L. V. Wang, and G. M. Lanza, "Near infrared photoacoustic detection of sentinel lymph nodes with gold nanobeacons," Biomaterials **31**, 4088-4093 (2010).
21. E. Z. Zhang, J. G. Laufer, R. B. Pedley, and P. C. Beard, "In vivo high-resolution 3D photoacoustic imaging of superficial vascular anatomy," Phys. Med. Biol. **54**, 1035-1046 (2009).
22. J. Xia, J. Yao, and L. V. Wang, "Photoacoustic tomography: principles and advances," Electromagnetic waves (Cambridge, Mass.) **147**, 1-22 (2014).
23. S. Hu, "Listening to the Brain With Photoacoustics," IEEE Journal of Selected Topics in Quantum Electronics **22**, 6800610 (2016).
24. J. Y. Kim, C. Lee, K. Park, G. Lim, and C. Kim, "Fast optical-resolution photoacoustic microscopy using a 2-axis water-proofing MEMS scanner," Sci. Rep. **5**, 07932 (2015).
25. C. Zhang, K. Maslov, S. Hu, R. Chen, Q. Zhou, K. K. Shung, and L. V. Wang, "Reflection-mode submicron-resolution in vivo photoacoustic microscopy," J. Biomed. Opt. **17**, 020501 (2012).
26. M. Moothanchery, A. Sharma, and M. Pramanik, "Switchable Acoustic and Optical Resolution Photoacoustic Microscopy for in vivo small-animal blood vasculature imaging," Journal of Visualized Experiments, e55810 (2017).
27. M. Moothanchery and M. Pramanik, "Performance Characterization of a Switchable Acoustic and Optical Resolution Photoacoustic Microscopy System," Sensors **17**, 357 (2017).
28. "American National Standard for Safe Use of Lasers," ANSI Standard Z136.1-2007, NY (2007).
29. G. Ma and C. Wu, "Microneedle, bio-microneedle and bio-inspired microneedle: A review," Journal of Controlled Release **251**, 11-23 (2017).
30. M. E. Wieder, D. C. Hone, M. J. Cook, M. M. Handsley, J. Gavrilovic, and D. A. Russell, "Intracellular photodynamic therapy with photosensitizer-nanoparticle conjugates: cancer therapy using a 'Trojan horse'," Photochemical & Photobiological Sciences **5**, 727-734 (2006).
31. D. C. Hone, P. I. Walker, R. Evans-Gowing, S. FitzGerald, A. Beeby, I. Chambrier, M. J. Cook, and D. A. Russell, "Generation of Cytotoxic Singlet Oxygen via Phthalocyanine-Stabilized Gold Nanoparticles: A Potential Delivery Vehicle for Photodynamic Therapy," Langmuir **18**, 2985-2987 (2002).
32. H. J. Kwon, Y. Byeon, H. N. Jeon, S. H. Cho, H. D. Han, and B. C. Shin, "Gold cluster-labeled thermosensitive liposmes enhance triggered drug release in the tumor microenvironment by a photothermal effect," J. Control. Release **216**, 132-139 (2015).

33. L. Poon, W. Zandberg, D. Hsiao, Z. Erno, D. Sen, B. D. Gates, and N. R. Branda, "Photothermal Release of Single-Stranded DNA from the Surface of Gold Nanoparticles Through Controlled Denaturating and Au−S Bond Breaking," Acs Nano **4**, 6395-6403 (2010).
34. A. K. Jain, C. H. Lee, and H. S. Gill,"5-Aminolevulinic acid coated microneedles for photodynamic therapy of skin tumors," J. Control. Release **239**, 72-81 (2016).
35. A. Taruttis, A. C. Timmermans, P. C. Wouters, M. Kacprowicz, G. M. v. Dam, and V. Ntziachristos, "Optoacoustic Imaging of Human Vasculature: Feasibility by Using a Handheld Probe," Radiology **281**, 256-263 (2016).
36. K. Park, J. Y. Kim, C. Lee, S. Jeon, G. Lim, and C. Kim, "Handheld Photoacoustic Microscopy Probe," Sci. Rep. **7**, 13359 (2017).
37. L. Lin, P. Zhang, S. Xu, J. Shi, L. Li, J. Yao, L. Wang, J. Zou, and L. V. Wang, "Handheld optical-resolution photoacoustic microscopy," J. Biomed. Opt. **22**, 041002 (2017).
38. T. Jin, H. Guo, H. Jiang, B. Ke, and L. Xi, "Portable optical resolution photoacoustic microscopy (pORPAM) for human oral imaging," Opt. Lett. **42**, 4434-4437 (2017).
39. P. Hai, J. Yao, K. I. Maslov, Y. Zhou, and L. V. Wang, "Near-infrared optical-resolution photoacoustic microscopy," Opt. Lett. **39**, 5192-5195 (2014).
40. Y. Zhang, J. Yu, A. Kahkoska, and Z. Gu, "Photoacoustic Drug Delivery," Sensors **17**, 1400 (2017).
41. J. Xia, C. Kim, and J. F. Lovell, "Opportunities for Photoacoustic-Guided Drug Delivery," Curr. Drug Targets **16**, 571-581 (2015).

1. Introduction

Microneedles (MN) are minimally invasive transdermal drug delivery platforms [1, 2]. This technology creates micropores in the stratum corneum, which enables the transdermal delivery of a broad range of therapeutics that cannot permeate intact skin [3]. Compared to MN made of metal, ceramics and silicon, polymeric MN are gaining attention due to their nontoxicity, biodegradability, biocompatibility, and easy fabrication [4].

In the design and development of the MN, it is often necessary to visualize and characterize the MN penetration, dissolvation or swelling, and biodegradation as well as the drug release profile and distribution in skin. Currently, researchers rely mainly on *ex vivo* techniques such as biopsy and histological staining. However, these methods are cumbersome and time-consuming, requiring the excision and processing of tissue specimens. In addition, the results derived with such destructive methods are often inaccurate as skin tissue is elastic and usually do not retain the microstructure generated during MN intrusion. Therefore, imaging technologies that provide real-time, non-invasive, *in situ* or *in vivo* images of the MN penetration and swelling in skin are highly desired.

Optical coherence tomography (OCT) is a commonly utilized optical imaging tool in MN-based studies, and has been illustrated in real time studies to visualize and monitor MN dissolution and swelling in skin [5-7]. However, this technique is limited by its shallow imaging depth and poor contrast between the MN and the skin tissue [8]. In a particular MN study by Tsai *et al.* OCT was implemented to study MN penetration and dissolution but to observe the drug release profile of an encapsulated drug fluorescence microscopy was used [9]. In similar OCT studies, post-processing of images using false colors was performed to evaluate MN penetration and dissolution [10]. Thus, alternative imaging tools which can provide real time characterization of drug release profiles induced by MN is critical in supplementing the growing potential of MN based drug delivery systems.

Photoacoustic Microscopy (PAM) is a fast-growing hybrid *in vivo* imaging modality combining optical contrast with ultrasound resolution [11-17]. It provides penetration beyond optical mean free path (~1 mm in skin) with high resolution (a lateral resolution within tens of microns and an axial resolution within hundreds of microns) and has been successfully applied to *in vivo* structural, functional, molecular, and cell imaging [16, 18-21]. In this process, PAM utilizes a short laser pulse to irradiate the tissues. There will be a temperature rise due to absorption of light by the tissue chromophores (such as melanin, red blood cells, water etc.),

which in turn produces pressure (acoustic waves) waves. A wideband ultrasonic transducer receives the acoustic signal outside the tissue boundary for reconstructing the optical absorption map inside the tissue. PAM overcomes the limitations of other existing optical modalities, combining optical contrast with ultrasound resolution. In PAM, the resolution is not limited by optical diffusion due to multiple photon scattering whereas contrast is related to the optical properties of the tissue. Unlike optical coherence tomography, diffuse optical tomography and fluorescence tomography, PAM does not rely on ballistic or backscattered light. Any light, including both singly and multiply scattered photons, contributes to the imaging signal. As a result, the imaging depth in PAM is relatively large. PAM has the ability to penetrate deeper and sustain high spatial resolution. Compared with ultrasonic imaging, PAM has rich intrinsic and extrinsic optical contrasts and is free of speckle artifacts [22].

PAM can be classified into acoustic resolution photoacoustic microscopy (AR-PAM) and optical resolution photoacoustic microscopy (OR-PAM). In AR-PAM deep tissue imaging can be achieved with weak optical and tight acoustic focusing. Resolving single capillaries acoustically will need ultrasonic transducers greater than 400 MHz central frequency; but at this frequency the penetration depth will be less than 100 µm. Therefore, tight optical focusing has been used in OR-PAM to achieve higher spatial resolution. OR-PAM can resolve single capillaries or even a single cell [23], and a lateral resolution up to 0.5 µm has been achieved [17, 24, 25]. Although the penetration depth of OR-PAM is limited due to light focusing, it can still image up to a maximum of 1.2 mm inside the biological tissue [17].

We hypothesize that OR-PAM can be used to observe the penetration of MN through skin and simultaneously observe the transdermal delivery of therapeutics. As a proof-of-concept, we first study the skin penetration of PMMA MN using OR-PAM. Then using gold nanoparticles (AuNPs) as a model drug, we examine the penetration, diffusion, and distribution of AuNPs in mice skin (*in vivo*) after the MN-assisted delivery.

2. Materials and methods

All chemical reagents unless specifically mentioned were obtained from Sigma-Aldrich (Singapore) and used without any modification.

2.1 Fabrication and characterization of AuNPs coated MN arrays

The MN were designed by Micropoint Technologies Pte Ltd (Singapore) using poly(methyl methacrylate) (PMMA) polymer in a 10×10 array with height of 600µm and base width of 300µm. PMMA polymer was chosen for its safety and high mechanical toughness to withstand MN compression when inserted into skin. Briefly, the fabrication methodology involved an injection molding process with an injection melt temperature of 293˚C, mold temperature between 60-120˚C, injection velocity of 150 mm/s and hold pressure of 48 MPa.

The PMMA MN were coated with 100 nm AuNPs. Briefly, the surface of the PMMA MN was thoroughly washed with acetone and blown dry with nitrogen gas. The MN surface was then plasma treated using Harrick Plasma Cleaner PDC 32G. The MN were dipped into 0.1 ml of concentrated AuNPs solution for several times ensuring that the solution covered the surface of the MN and was dried in the oven at 80° C overnight.

To evaluate the MN skin insertion ability, MN patches were inserted into treated fresh porcine skin using an applicator and removed after 1 minute retention. Later, the skin tissue was fixed and stained using Hematoxylin and Eosin (H&E) for histological analysis.

2.2 Optical resolution photoacoustic microscopy system

The OR-PAM system [Fig. 1] employs a nanosecond tunable laser system; consist of a diode-pumped solid-state Nd-YAG laser and a dye laser. The laser system can be tunable between 559 nm-576 nm. The laser beam was reshaped by an iris and then spatially filtered by a combination of condenser lens, CL (LA4327, Thorlabs) and a 50 μm pinhole, PH (P50S, Thorlabs). The attenuated beam through a variable neutral density filter, NDF (NDC-50C-4M), was launched on to a single-mode fiber, SMF (P1-460B-FC-1, Thorlabs) using a fiber coupler, FC (F-91-C1, Newport). The beam out from the SMF was collimated by an Achromatic lens, L1 (32-317, Edmund Optics), reflected by a stationary elliptical mirror, M and filled the entire back aperture of another identical Achromatic lens, L2. The focusing beam will be passed through a optoacoustic beam combiner which consist of a right angled prism, RA (PS615, Thorlabs) and a rhomboid prism, RP (47-214, Edmund optics) with a layer of silicon oil, SO (DMPS1M, Sigma Aldrich) in between. The silicon oil layer acts as acoustic reflective and optical transparent film. An acoustic lens, AL (LC4573, Thorlabs) was attached at the bottom of the rhomboid prism provided acoustic focal diameter ~46 μm. The ultrasonic transducer (UST), 50 MHz center frequency was placed on top of the rhomboid. The optical and acoustic foci were aligned confocally to maximize the detection sensitivity. The laser repetition rate for the OR-PAM was set to 5 kHz and the laser energy at focus can be varied up to 200 nJ per pulse. The laser wavelength was set at 570 nm.

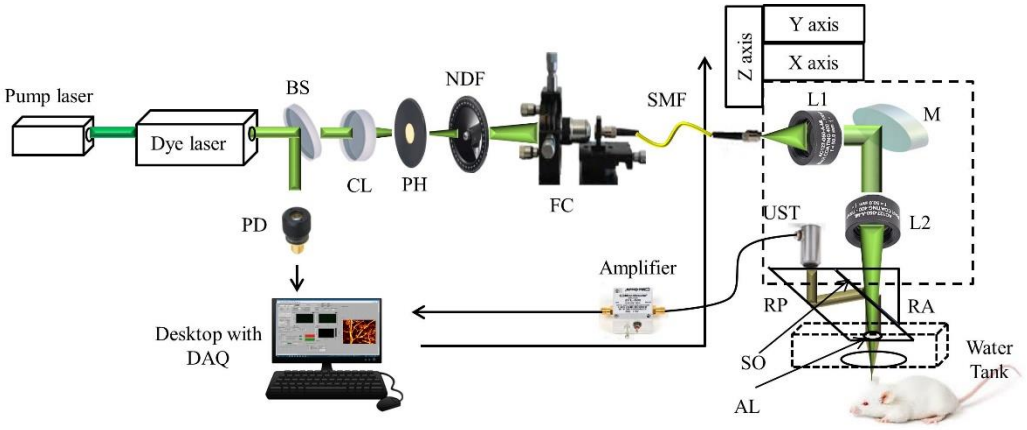

Fig. 1. Schematic of the optical resolution photoacoustic microscopy imaging system. BS - Beam Sampler, CL - Condenser lens, PH – Pinhole, NDF- Neutral density filter, PD – photodiode, FC – Fiber coupler, SMF - Single mode fiber , L1&L2 - Achromatic lens, M - Mirror, UST – Ultrasound transducer, DAQ - Data acquisition card,, RA - Right angle prism, RP - Rhomboid prism, , SO – Silicon oil, AL - Acoustic lens.

The OR-PAM scanner head was attached to a 3-axis motorized stage connected to the computer. For photoacoustic imaging the bottom of the OR-PAM scanner head was submerged in a water-filled tank. For optical and acoustic transmission an imaging window (7 cm x 7 cm) was opened in the bottom of the tank and sealed with a polyethylene membrane. The PA signal acquired by the UST was amplified by two 24 dB amplifiers (ZFL-500LN, Mini Circuits), and was recorded in a desktop computer using a data acquisition card, DAQ. The scanning and data acquisition was controlled using Labview software. The synchronization of the data acquisition and the stage motion was controlled through the signal from a photodiode, PD. Two-dimensional continuous raster scanning of the imaging head was used during image acquisition. This OR-PAM system has a spatial resolution of ~4.2 micron, axial resolution of ~33 micron, and an imaging depth up to ~1.4 mm as characterized previously [26, 27].

2.3 Laser safety

For *in vivo* imaging, according to American National Standards Institute (ANSI) laser safety standards [28], the maximum pulse energy by a single laser pulse (MPE_{SP}) on the skin surface shouldn't exceed $MPE_{SP} = 2.C_A \times 10^{-2}\,J/cm^2$, where C_A the wavelength correction factor, unity for visible wavelength range (400-700 nm). If a point on skin is exposed to more than 10 sec the irradiance shouldn't exceed 200 mW/cm^2. In the case of raster scanning a point on the skin won't be exposed for 10 sec, hence the maximum permissible exposure (MPE_{AVG}) is limited by $1.1C_A\ t^{0.25}$ in mJ/ cm^2 where t denotes the exposure duration in seconds. For OR-PAM we believe due to optical aberrations at the prism surface and acoustic lens objective NA might have reduced the from 0.11 to 0.075. Assuming the optical focus is 150 micron below the skin surface for *in vivo* imaging, the surface spot size was 22.5 µm in diameter and the calculated optical fluence for a single laser pulse was 20.4 mJ/cm^2 (90 nJ/pulse) close to the safety limit. Having a minimum pixel separation of 2 µm, an average of 11 (N) adjacent laser pulses overlaps on the skin surface. At 5 kHz LRR the exposure time is 2.4 ms. So the MPE_{TRAIN} was 238 mJ/cm^2.The MPE_{SP} for the pulse train was (MPE_{AVG}) = MPE_{TRAIN} / N = 238 /11 = 21.6 mJ/cm^2 close to the maximum permissible limit.

2.4 Imaging methodology

The ear of a female mice of body weight 25 g and age 4 weeks, procured from InVivos Pte. Ltd. Singapore, were used in the imaging experiments. Animal experiments were performed according to the approved guidelines and regulations by the institutional Animal Care and Use committee of Nanyang Technological University, Singapore (Animal Protocol Number ARF-SBS/NIE-A0263). The animals were anesthetized using a cocktail of Ketamine (120 mg/kg) and Xylazine (16 mg/kg) injected intraperitoneally (dosage of 0.1 ml/10 gm). After removing hair from the ear the mouse was positioned on a microscopic glass slide before the MN coated with AuNPs was pressed into a mouse ear using an applicator. MN was inserted into mouse ear for 60 seconds and removed before OR-PAM imaging was performed. Mouse ear was used as a suitable model to mimic the human epidermis thickness. In addition, the planar surface of the mouse ear tissue enables uniform pressure to be applied during MN insertion to ensure fair distribution of AuNPs in the treated region for effective monitoring of AuNPs delivery. The animal was further anesthetized with vaporized isoflurane system (1 L/min oxygen and 0.75% isoflurane) during the imaging period. The imaging region was made in contact with the polyethylene membrane using ultrasound gel. In order to characterize the penetration depth as well as the rate of diffusion of AuNPs at each depth, a smaller region of interest (1.5 mm × 0.75 mm) was scanned at different time intervals after MN insertion with a step size of 2 µm along X-axis and 4 µm long Y-axis. A 2 mm × 1.25 mm untreated area of the mouse ear was imaged as a control image with a step size of 2 µm along X-axis and 5 µm along Y-axis.

3. Results and discussion

3.1 AuNPs coated MN array

The fabricated MN array has a dimension of 1 cm by 1 cm with solid MN tips of height 600 µm and base width of 350µm [Figs. 2(a) and 2(b)]. The PMMA MN could easily penetrate the fresh porcine skin tissue to a depth of 400µm as observed in the H&E staining, in which MN tip reached the dermis layer [Fig. 2(c)]. The difference between the needle length and the actual penetration depth (displacement) should be due to the elasticity of skin [29]. The observed penetration depth is enough for effective intradermal drug delivery in humans.

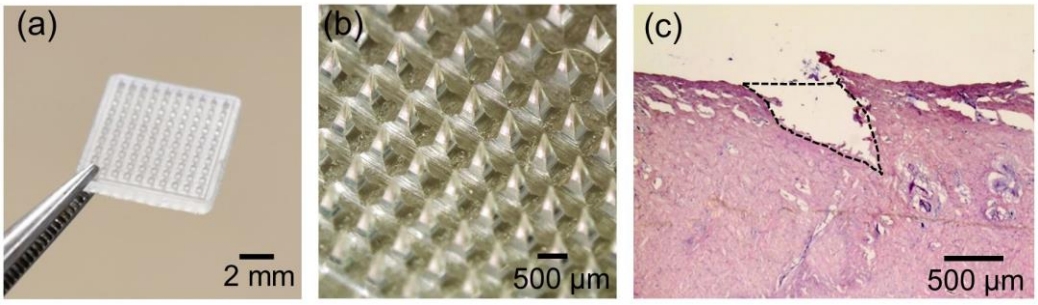

Fig. 2. Characterization of PMMA MN patch: (a) camera image of the PMMA MN patch; (b) close view of the MN array on the patch under optical microscope; (c) H&E staining of porcine skin treated with PMMA MN patch.

In this study, AuNPs are taken as the model drugs for MN mediated transdermal delivery. AuNPs are capable of enhancing singlet oxygen generation and have shown to improve the efficacy of conventional photodynamic therapy [30, 31]. Hence, AuNPs can be used as potential therapeutic agents to destroy tumor cells [32, 33]. They were coated on PMMA MN via facile dip-coating. The coated MN kept the same morphology as before [Fig. 3(a)]. At a greater magnification, clusters of AuNPs can be observed on the pyramidal sides of the MN tips [Fig. 3(b)]. Taking together, the dip-coating successfully coated MN with AuNPs without influencing the structural integrity of the MN.

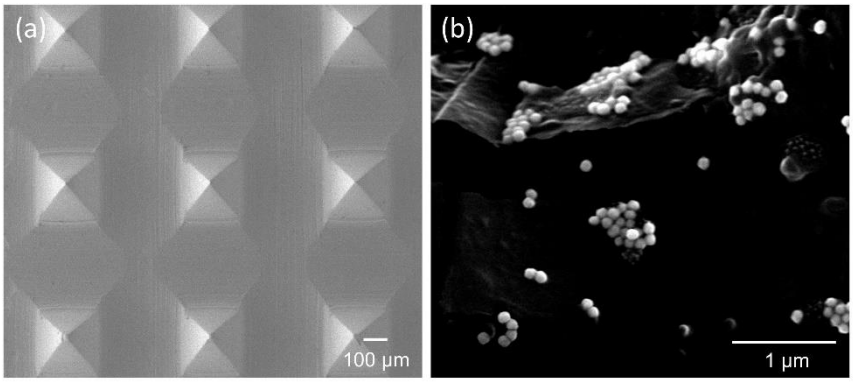

Fig. 3. SEM characterization of AuNPs coated PMMA MN: (a) A top view; (b) Zoom-in visualization of the AuNPs on a coated PMMA MN.

3.2 Photoacoustic imaging of the skin penetration of MN

To study the penetration effects of MN, firstly an image of the blood microvasculature in the mouse ear was obtained under the Maximum Amplitude Projection (MAP) OR-PAM [Figs. 4(a) and 4(b)]. A control image taken [Fig. 4(a)] before the MN treatment shows the blood vessel structures present inside the mouse ear. Following the insertion of AuNPs coated MN, certain areas of the microvasculature [white dotted box, Fig. 4(b)], were observed to have nanoparticle deposition in a patterned way similar to the arrangement of the MN tips in the designed MN array. As AuNPs have a strong optical absorption (resulting in strong photoacoustic signal), monitoring the delivery of these particles in the skin after the detachment from the MN is easily achieved. This concludes the successful MN penetration and delivery of the AuNPs using the MN. In addition, it is also notable that no visible damage to the blood vessels structure was observed following the MN intervention.

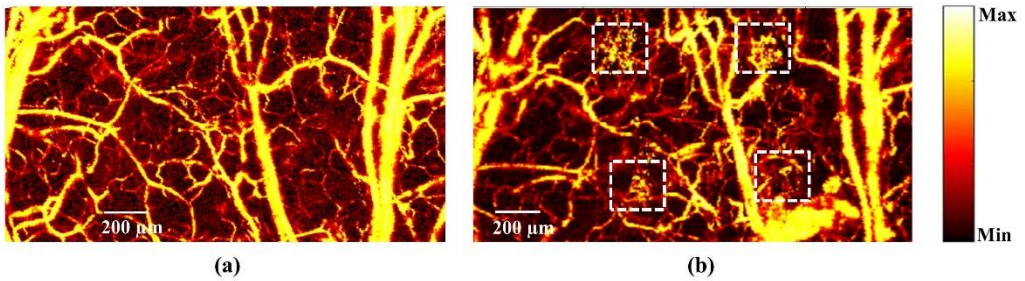

Fig. 4. *In vivo* photoacoustic imaging of mouse ear (a) before and (b) after the AuNPs coated MN insertion.

Next, MAP photoacoustic images at different time intervals (after the MN insertion) of 5 minutes, 40 minutes, 95 minutes, and 145 minutes were obtained as shown in Figs. 5 (a) -5(d), respectively. Using these images, we observe the real-time diffusion process of the AuNPs in the tissue. With time progression, a lesser photoacoustic signal intensity is observed indicating a decreasing diffusion flux. To quantify the penetration depth of the AuNPs, Fig. 5(a) was segmented into image stacks in increasing depth from the skin surface as shown in Fig. 5(e). Herein, we can clearly visualize the accumulation of the nanoparticles along the z-axis of the tissue in different concentrations. Up to a depth of 150 µm in mice ear tissue, we confirm the deposition of the nanoparticles using MN delivery.

To quantify the observations from the MAP images as shown in Figs. 5(a) – 5(d), the photoacoustic (PA) signal amplitude is studied. The reduction in the PA signal amplitude with time at the areas of AuNPs accumulation can be interpreted as decreased nanoparticles diffusion. The rate of diffusion of AuNPs with time and along the depth profile was measured using the average PA signal amplitude of a small region of interest (0.4 mm×0.4 mm shown in white dotted area) at different time intervals and at different depths. Figure 5(f) shows the plot of average PA signal amplitude with time and depth. The maximum PA amplitude was attained immediately after MN insertion at each of the measured depths and reduced significantly with time. In addition, the rate of diffusion was significant in the first 90 minutes following MN insertion and no significant decrease in the PA amplitude was observed thereafter. These results can be well understood with Fick's First Law of Diffusion; which states that particles diffuse with a flux proportional to the concentration gradient. As time progressed, the AuNPs diffused laterally in a steady state and hence at each of the depth, we observe a similar trend in the PA signal. The PA amplitude signal measured at the surface of the tissue is comparable to the signal attained at a depth of 180 µm. This can be explained by the limitation of the sampled tissue as the mice ear has a thickness of 150-170 µm.

The fast diffusion process of AuNPs (approximately ~20 minutes) inside the tissue indicates that it can be an ideal candidate for photodynamic therapy [34]. On the contrary, therapeutics delivered intravenously can potentially elicit toxicity to normal cells and cause severe side effects. As such, MN can be explored as an improved target specific therapeutic delivery tool. To use MN in a photosensitizing drug delivery platform, it is important to visualize and characterize the MN properties including penetration depth, dissolution in skin as well as the drug release profiles. Photoacoustic imaging has already shown potential towards clinical translations [35] and the feasibility for making portable handheld devices makes PAM a promising imaging tool for clinical translations [36-38]. Photoacoustic microscopy can help in *in vivo* monitoring of these parameters and thus may play an important role in the development of drug coated MN therapy.

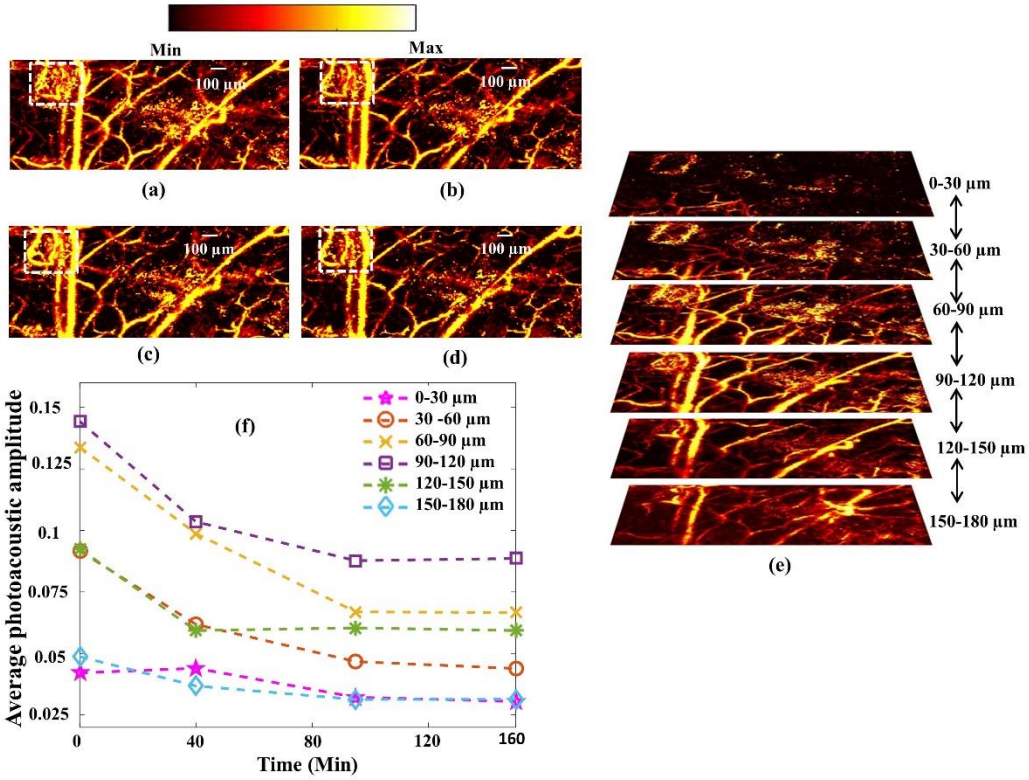

Fig. 5. *In vivo* photoacoustic microscopy (Maximum amplitude projection) image of mouse ear; data acquisition started (a) 5 Min, (b) 40 Min, (c) 95 Min, and (d) 150 Min after AuNPs coated microneedle insertion. (e) Image slices of (a) at various depths. (f) Variation of photoacoustic signal amplitudes over time for various depths.

Although most OR-PAM system use visible wavelength for imaging blood vasculature, near infrared (NIR) wavelength window can provide much deeper imaging (up to 3.2 mm), due to the reduced scattering and absorption by the tissue [39]. Therefore, NIR OR-PAM systems can also be used for monitoring *in vivo* nanoparticle delivery using MN. We have selected AuNPs having absorption in the 570 nm wavelength as the model drug in this study. The technology can be used for different drug delivery monitoring by choosing appropriate drug having absorbance in the specific wavelength of the laser used. Numerous drug carriers have capability of providing strong PA signals, including carbon nanotubes, gold nanoparticles, porphysomes etc. By loading conventional drugs into these nanocarriers, the nanocarrier can be non-invasively imaged and assessed. Another way is to co-load drugs of interest with small molecule NIR dyes into a common carriers [40, 41]. A detailed study by using NIR laser and gold nanorods (or other nanocarriers) as the model drug using different MN needs to be carried out to demonstrate better visualization of maximum penetration depth and drug delivery.

4. Conclusion

For the first time, we reported the use of OR-PAM to study the MN skin penetration and delivery of AuNPs *in vivo* using mice model. We can see that MN were able to efficiently penetrate skin tissue and deliver the AuNPs up to a depth of ~150 µm. The diffusion pattern of delivered AuNPs in the skin tissue was observed and found to take ~90 minutes post the MN insertion. This work reveals the potential use of photoacoustic microscopy in the in vivo monitoring of transdermal drug delivery using MN platforms.

Acknowledgements

The authors would like to acknowledge Dr. Dhiman Das for valuable discussion and help in coating AuNPs to MN.

Funding

The authors would also like to acknowledge the financial support from Tier 2 grant funded by the Singapore Ministry of Education Tier-2 Academic Research Funds (ARC2/15: M4020238 to M.P.), Singapore Ministry of Education Tier-1 Academic Research Funds (RG 131/15 to C.J.X.), NTU-Northwestern Institute for Nanomedicine (M4081502.F40 to C.J.X.).

Disclosures

The authors declare that there are no conflicts of interest related to this article.